# Coordinated Multi-loop Control Design of VSM-controlled DFIGs in Wind Farm to Tackle Intra-machine Controller Interactions

Javier García-Aguilar, Aurelio García-Cerrada, *Senior Member, IEEE*, Juan L. Zamora, Emilio J. Bueno, *Senior Member, IEEE,* Elena Saiz, Almudena Muñoz-Babiano, and Mohammad E. Zarei

***Abstract*—The displacement of synchronous generators by converter-interfaced renewable energy sources requires wind farms to provide inertia, damping, and voltage support, particularly in increasingly weak grids. Based on classical frequency-domain loop-shaping techniques, this paper presents a coordinated multi-loop control design methodology for virtual synchronous machine (VSM)-controlled doubly-fed induction generators (DFIGs) in a wind farm to tackle the intra-machine controller interactions. Starting from an initial design and a full small-signal linearisation, the procedure redesigns every local open loop to meet explicit phase margin targets through a single and prioritised iteration. The resulting controllers achieve step responses and stability margins close to those programmed at the design stage, despite the cross coupling between control loops. Results can be improved further if a few more design iterations are carried out. Since the controller synthesis relies exclusively on classical loop-shaping tools available in commercial simulation suites, it is directly applicable to industrial-scale projects.**

***Index Terms*—Doubly-fed induction generator (DFIG), frequency-domain analysis, grid-forming (GFM) control, multi-loop control, small-signal stability, virtual synchronous machine (VSM), weak grid.**

## I. Introduction

TYPE-III wind turbines based on doubly-fed induction generator (DFIG) currently dominate the installed wind capacity (mainly onshore), as they enable the variable-speed operation with reduced costs [1]. Traditionally, the grid-following (GFL) technology, which uses a phase-locked loop (PLL) for grid synchronisation, has dominated the DFIG-based generation. Specifically, an inner rotor-side current loop controls the electromagnetic torque, while outer loops of the grid-side converter (GSC) regulate the DC-link voltage and stator-terminal reactive power [2]. In strong grids, this configuration operates effectively because the voltage at the point of common coupling (PCC) is barely affected by the operation actions of DFIG. However, in weak grids or during parallel DFIG operation, this configuration is prone to adverse cross-couplings and PCC voltage variations, which can trigger torsional and sub-synchronous modes [3].

Grid-forming (GFM) control has emerged as a key enabler for a high penetration of converter-interfaced generation (CIG) in general [4], and is now being mandated for DFIGs. Among the GFM control strategies, the virtual synchronous machine (VSM) emulates the swing equation and electromagnetic behaviour of a synchronous generator, thereby providing the so-called virtual inertia and damping [5]. Recent publications have demonstrated that the DFIG can also operate in the GFM mode without compromising their cost advantages [6]. However, in most existing GFM-based implementations, a VSM power loop is simply overlaid on the inner current and voltage loops, with the assumption that the inner layers work seamlessly. Unfortunately, this hypothesis no longer holds with low short-circuit ratio (SCR) ($SCR \leq 2$) or when multiple DFIGs share a collector feeder [7], [8]. In such cases, the impact of the time response of the inner loops on the outer loops should not be underestimated.

The small-signal and impedance-based analyses have revealed the root causes of instabilities in GFM-based DFIGs. The aggressive power-angle modulation by the VSM outer loop is affected by the limited yet fast response speed of the rotor-side current controllers, especially when the PLL or stator-flux observer introduces additional delays [9]-[11]. The problem is exacerbated by unequal collector impedances in multi-machine systems and power-line resonances [12].

Manuscript received: July 11, 2025; revised: December 1, 2025; accepted: March 10, 2026. Date of CrossCheck: March 10, 2026. Date of online publication: XX XX, XXXX.

This work was supported by Research Project funded by ASOCIACIÓN/COLEGIO NACIONAL DE INGENIEROS DEL ICAI, the European Regional Development Fund, The Spanish Ministry of Science, Innovation and Universities (MICIU) and the Spanish State Research Agency (AEI) in collaboration with Siemens Gamesa, and Siemens Gamesa Renewable Energy Innovation & Technology S. L. (No. RTC-2017-6074-3) and the Research Project funded by MICIU and AEI (No. PID2024-158935OB-C21).



J. García-Aguilar, A. García-Cerrada (corresponding author), and J. L. Zamora are with Institute for Research in Technology, Comillas Pontifical University, Madrid, Spain (e-mail: jgaguilar@comillas. edu; aurelio. garcia@comillas. edu; zamora@comillas.edu).

E. Bueno is with Alcalá University, Madrid, Spain (e-mail: emilio.bueno@uah. es).

E. Saiz, A. Muñoz-Babiano, and M.E. Zarei are with Siemens Gamesa Renewable Energy Innovation & Technology S.L, Madrid, Spain (e-mail: elena. saiz@siemensgamesa. com; almudena. munoz@siemens-energy. com; mohammad. zarei@siemens-energy.com).

DOI: 10.35833/MPCE.2025.000640

In this regard, the recent literature addresses the co-ordinated tuning of all relevant control loops, i.e., current, DC-link, power, voltage, and PLL loops, in all forms of CIG including DFIG-based generation. In fact, important organizations in the power system industry such as IEEE [13], ENTSO-E [14], and CIGRE [15] have warned of dangerous interactions—both among converter controllers and between traditional synchronous generators and converter controllers. Therefore, it is of special concern to detect, analyse, and mitigate such interactions.

Reference [16] discusses the tuning of the proportional-integral (PI) control parameters of both the inner and outer loops in a full-converter-type wind turbine, aiming to achieve an optimal response to power oscillations. However, this study develops an aggregated model for the wind turbines and fails to elaborate on the interaction between the designed control loops.

Techniques such as $H_\infty$ optimisation and $\mu$-synthesis enable robust control design and have been applied to single converters [17], [18] and further extended to multi-converter systems [19] - [21]. However, such techniques often yield high-order controllers, which impose a substantial computational burden for large multi-machine systems. Additionally, the tuning process often compromises physical interpretability. Similarly, the time-domain optimisation methods, while capable of handling non-linearities and complex constraints [22], tend to be sensitive to model accuracy and struggle with guaranteeing prescribed frequency-domain performance metrics such as phase and gain margins across coupled control loops. Multivariable techniques in the process-control domain have also been adapted to wind turbines [23], [24], but without further development.

Based on the classical frequency-domain loop-shaping techniques, this paper proposes a coordinated multi-loop control design methodology for VSM-controlled DFIGs in a wind farm. The design procedure accounts for intra-machine controller interactions to avoid discrepancies between the achieved and expected design performance. Unlike recent automated $H_\infty/\mu$ tuning, the proposed methodology gives direct control over individual loop characteristics including phase and gain margins through an iterative and physically-grounded process. This could facilitate the interpretation and tuning for practising engineers.

The main contributions of this paper can be summarised as follows.

1) A methodology based on the full small-signal linearisation is proposed, which captures the intra-machine controller interactions in DFIGs.

2) A classical frequency-domain loop-shaping technique, implemented through a single and prioritised iteration across all controllers in each DFIG, prevents the deterioration of the stability margins of the open-loop frequency response due to intra-machine controller interactions and unequal collector impedances for individual DFIGs. A few additional iterations recover the original specifications with very high precision.

3) The proposed methodology relies solely on classical loop-shaping tools available in commercial simulation software, enabling its direct application to industry-scale projects.

4) The proposed methodology is readily applicable to conventional PI controllers, the most common type in DFIG-based wind power applications, further facilitating its industrial application.

These contributions are validated by detailed simulation on an 8.4 MW four-machine benchmark system.

The remainder of this paper is organised as follows. Section II models the four-machine benchmark system. Section III introduces the initial tuning. Section IV illustrates the intra-machine controller interactions. Section V presents the coordinated multi-loop control design methodology. Section VI provides the results and validation of the proposed methodology, Section VII quantifies the performance improvement, and Section VIII concludes this study.

## II. Modelling of Four-machine Benchmark System

Figure 1 shows the four-machine benchmark system in this work. This system consists of four identical Type-III wind turbines based on DFIG, each with a rated power of 2.1 MW, which are connected in parallel to the 33 kV transmission grid via collector feeders and step-up transformers.

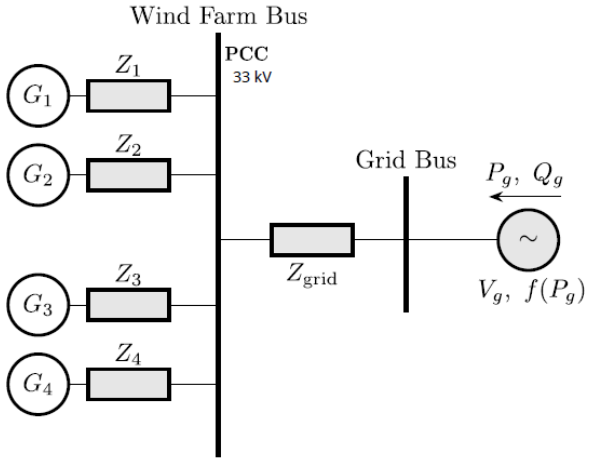


Fig. 1. Single-line diagram of four-machine benchmark system.

The impedances of the four collector-transformer combinations $Z_1$-$Z_4$ are intentionally made non-uniform: $Z_1 = Z_2 = 0.06$ p. u. and $Z_3 = Z_4 = 0.12$ p. u., both of which are inductive. These per-unit values incorporate the equivalent impedances of cable and switchgear for each collector feeder as well as the step-up transformer of each DFIG. The PCC is linked to an equivalent grid bus via a lumped inductive Thevenin impedance $Z_{\text{grid}}$. At the PCC, $SCR = 1$, which means that the short-circuit power of the grid is equal to the nominal power of the 8.4 MW four-machine benchmark system, and $Z_{\text{grid}} \approx$ j0.14 p.u.. A detailed explanation of the base values and the derivation of $Z_{\text{grid}}$ can be found in Supplementary Material A. This models an extremely weak grid, while maintaining a tractable model for detailed frequency-domain analysis.

Unless otherwise stated, all equations and electrical/mechanical variables are expressed in p. u. based on the base values detailed in Supplementary Material A. Network and

passive elements are represented in a synchronous *dq* reference frame as complex numbers. The *d*-axis of this frame, which establishes the unified global *dq* reference frame for the entire system simulation, is aligned with the space vector of grid voltage using the power-invariant Park transformation. Therefore, the grid voltage is defined as $v_g = 1\angle 0^{\circ}$. In this paper, the subscripts $(\cdot)_d$ and $(\cdot)_q$ are the *d*- and *q*-axis components for vectors, respectively, or real and imaginary parts for complex numbers.

### A. External Grid Model

The external grid is modelled with a fixed root mean square (RMS) magnitude of grid voltage ($|v_g| = 1$ p.u.), but with a time-varying frequency $f = \omega_g/\omega_b$, where $\omega_g$ is the instantaneous grid angular frequency, and $\omega_b = 2\pi \times 50$ rad/s is the base value for the per-unit value of electrical angular speed.

Figure 2 depicts the simplified dynamic model of the external grid, where $P_m^{\star}$ is the mechanical power setpoint of equivalent generator; $P_m$ is the mechanical power delivered after the governor-turbine train dynamics; $P_g$ is the electrical power exported from the grid; $\tau_g$ is the governor time constant of equivalent generator; $H_g$ is the lumped inertia constant of external grid; $T_1$ and $T_2$ are the time constants for the turbine of equivalent generator; $G_t(s)$ is the second-order model representing turbine dynamics; and $D_{eq,g}$ is the equivalent damping coefficient of the external grid. In Fig. 2, the base power is 8.4 MVA, and the base frequency is 50 Hz. $D_{eq,g} = 20$ p.u., $H_g = 5$ s, $T_1 = 0.3$ s, $T_2 = 7$ s, and $\tau_g = 2$ s.

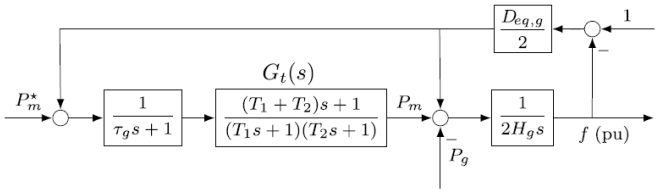


Fig. 2. Simplified dynamic model of external grid.

The feedback term $-(D_{eq,g}/2)\Delta f$ ($\Delta f \triangleq f - 1$) serves a dual role:

1) In the mechanical branch, which represents the governor-turbine response, the feedback term $-(D_{eq,g}/2)\Delta f$ provides the primary frequency control. By equating $-(D_{eq,g}/2)\Delta f$ to the classical static droop characteristic $\Delta P = -\Delta f/R_{\mathrm{eq}}$, we obtain the equivalent droop of the external grid: $R_{\mathrm{eq}} = 2/D_{eq,g}$.

2) In the electrical branch, the same feedback term $-(D_{eq,g}/2)\Delta f$ summarises the damping due to the natural frequency dependence of the connected power demand.

The simplified time-domain equations that describe the grid frequency dynamics are given as:

$$\tau_g \frac{dP_m}{dt} = -P_m + P_m^{\star} - \frac{D_{eq,g}}{2}\Delta f \tag{1}$$

$$2H_g \frac{d\Delta f}{dt} = P_m - P_g - \frac{D_{eq,g}}{2}\Delta f \tag{2}$$

Note that $G_t(s)$ has been incorporated into the overall state-space model, but is omitted from (1) for the sake of conciseness.

Denoting $\omega_i$ as the instantaneous electrical angular speed in the reference frame of any device *i* (such as reference frame of a generator stator, reference frame of a generator rotor, or internal frame of a GSC) and $\delta_i$ as the electrical angle of the reference frame of device *i* with respect to a unified global *dq* reference frame, the relationship between the two frames is given by:

$$\delta_i(t) = \delta_i(t_0) + \int_{t_0}^{t} \overbrace{[\omega_i(\tau) - \omega_g(\tau)]}^{\mathrm{d}\delta_i(t)/\mathrm{d}t} \mathrm{d}\tau \tag{3}$$

where *t* is the index of time; and $t_0$ is the initial simulation time.

At the steady-state operating point, $\omega_g(t_0) = \omega_b$, and by definition, the electrical angle of the unified global *dq* reference frame $\delta_g(t) \equiv 0$.

### B. DFIG Model

The DFIG model, with all variables in p.u., follows [1], which uses a *dq* reference frame synchronous with the space vector of stator voltage (i.e., synchronous speed) using the power-invariant Park transformation and can be expressed as:

$$\boldsymbol{u}_{dqs} = r_s \boldsymbol{i}_{dqs} + \mathrm{j}\omega_s \boldsymbol{\psi}_{dqs} + \frac{1}{\omega_b}\frac{\mathrm{d}\boldsymbol{\psi}_{dqs}}{\mathrm{d}t} \tag{4}$$

$$\boldsymbol{u}_{dqr} = r_r \boldsymbol{i}_{dqr} + \mathrm{j}(\omega_s - \omega_m)\boldsymbol{\psi}_{dqr} + \frac{1}{\omega_b}\frac{d\boldsymbol{\psi}_{dqr}}{dt} \tag{5}$$

where $\boldsymbol{u}_{dqs}$, $\boldsymbol{i}_{dqs}$, and $\boldsymbol{\psi}_{dqs}$ are the vectors of stator voltage, stator current, and stator flux linkage, respectively; $\boldsymbol{u}_{dqr}$, $\boldsymbol{i}_{dqr}$, and $\boldsymbol{\psi}_{dqr}$ are the vectors of rotor voltage, rotor current, and rotor flux linkage, respectively; $r_r$ is the rotor resistance; $\omega_s$ is the angular speed of the *dq* reference frame synchronous with the space vector of stator voltage; and $\omega_m$ is the electrical angular speed of rotor.

$\boldsymbol{\psi}_{dqs}$ and $\boldsymbol{\psi}_{dqr}$ are expressed as:

$$\begin{cases} \boldsymbol{\psi}_{dqs} = L_s \boldsymbol{i}_{dqs} + L_M \boldsymbol{i}_{dqr} \\ \boldsymbol{\psi}_{dqr} = L_M \boldsymbol{i}_{dqs} + L_r \boldsymbol{i}_{dqr} \end{cases} \tag{6}$$

where $L_s$ and $L_r$ are the stator and rotor inductances, respectively; and $L_M$ is the magnetising inductance of the DFIG.

The electric torque $T_e$ applied to the shaft in the positive direction of the rotor angular speed $\omega_r$ is:

$$T_e = \frac{1}{\sqrt{3}} L_M \mathrm{Imag}\left(\boldsymbol{i}_{dqs}\boldsymbol{i}_{dqr}^{*}\right) \tag{7}$$

The wind turbine blades are assumed to work with a pitch angle $\beta = 1^{\circ}$ and the wind turbine power coefficient is approximated as:

$$\begin{aligned} C_p(\lambda) = &-0.4958 + 0.2776\lambda - 0.02561\lambda^2 + \\ &8.7047\times 10^{-4}\lambda^3 - 1.1331\times 10^{-5}\lambda^4 \end{aligned} \tag{8}$$

where $\lambda$ is the ratio between the blade-tip speed and the wind speed. When $\lambda \approx 9$, $C_p$ reaches a maximum value of nearly 0.5.

The mechanical power extracted from the wind can be calculated as:

$$P_{mec}=\frac{1}{2}\rho\pi R^2 C_p(\lambda)v^3 \tag{9}$$

where $\rho$ is the air density; $R$ is the blade radius; and $v$ is the wind speed.

The electromechanical drivetrain for each turbine-generator set is simulated as the classical two-mass model:

$$\frac{d\omega_t}{dt}=\frac{1}{2H_t}\left[T_m-D_t\omega_t-T_{tg}-D_{tg}(\omega_t-\omega_r)\right] \tag{10}$$

$$\frac{dT_{tg}}{dt}=\omega_{m,b}K_{tg}(\omega_t-\omega_r) \tag{11}$$

$$\frac{d\omega_r}{dt}=\frac{1}{2H_g}\left[T_{tg}+T_e-D_q\omega_r+D_{tg}(\omega_t-\omega_r)\right] \tag{12}$$

where $T_m$ is the torque applied by the blades; $\omega_t$ is the mechanical angular speed of the blade-side shaft; $\omega_r$ is the mechanical angular speed of rotor; $\omega_{m,b}=\omega_b/N_{pp}$ is the base value of mechanical angular speeds, and $N_{pp}$ is the number of pole pairs; $D_t$ and $H_t$ are the friction and inertia of the blade-side mass; $D_g$ and $H_g$ are the friction and inertia of the DFIG-side mass; $D_{tg}$ is the friction coefficient between the blade-side and DFIG-side masses; $T_{tg}$ is the spring torque between the blade-side and DFIG-side masses; and $K_{tg}$ is the characteristic constant of that spring. All the parameters of this two-mass model and their conversion to per-unit values, as used in (10)-(12), are shown in Supplementary Material A.

### C. Control Architecture

A five-layer hierarchical control structure is implemented to each DFIG, as shown in Fig. 3, which includes: ① a virtual-shaft controller emulating synchronous machine inertia and damping characteristics for primary frequency support; ② a virtual-flux controller that decides the rotor current setpoint to regulate the magnitude of DFIG stator flux; ③ an inner rotor current controller for the rotor-side converter (RSC) (hereinafter referred to as RSC*dq* for simplicity), managing the *d*- and *q*-axis rotor currents; ④ a DC-link voltage controller, i.e., VDC, for the DC bus between the RSC and GSC; ⑤ an inner grid current controller for the GSC (hereinafter referred to as GSC*dq* for simplicity), regulating the *d*- and *q*-axis currents injected into the grid from GSC.

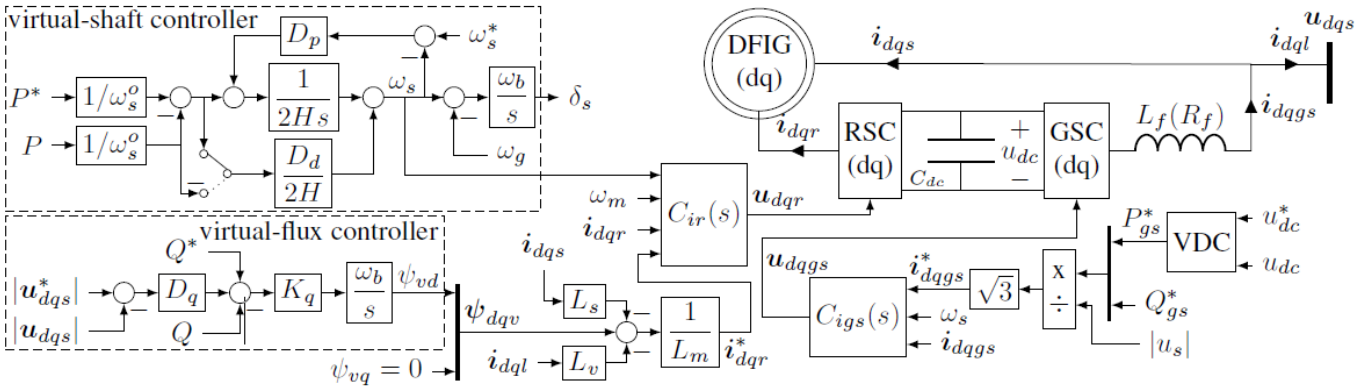


Fig. 3. Five-layer hierarchical control structure of DFIG.

In Fig. 3, $u_{dc}$ and $C_{dc}$ are the DC-link voltage and capacitor, respectively; $\boldsymbol{i}_{dqgs}$ is the vector of current injected into the grid from GSC; $\boldsymbol{i}_{dql}=\boldsymbol{i}_{dqgs}-\boldsymbol{i}_{dqs}$ is the vector of total current of DFIG; $\boldsymbol{u}_{dqgs}$ is the vector of output voltage of the GSC; $\boldsymbol{\psi}_{dqv}$ is the vector of virtual flux; $H$ is the virtual inertia time constant; $D_p$ and $D_d$ are the droop gain and damping coefficient of virtual-shaft controller, respectively; $D_q$ and $K_q$ are the droop gain and proportional gain of virtual-flux controller, respectively; $L_f$ and $R_f$ are the inductance and resistance of GSC filter, respectively; $L_v$ is the virtual inductance; $P$ and $Q$ are the actual active and reactive power delivered by the VSM, respectively; $\omega_s$ is the output frequency of VSM, i.e., the angular speed of the *dq* reference frame used in (4); $\omega_s^0$ is the initial output frequency of VSM; $C_{ir}(s)$ and $C_{igs}(s)$ are the transfer functions of RSC*dq* and GSC*dq*, respectviely; and $P_{gs}$ and $Q_{gs}$ are the active and reactive power delivered by the GSC, respectively; $\delta_i$ as the electrical angle of the reference frame of stator; and the superscript * represents the setpoint value.

In this study, the reactive power injection at the PCC by the GSC is disabled, i.e., $Q_{gs}^{\star}=0$.

The control structures of RSC*dq* and GSC*dq* for DFIG are shown in Fig. 4(a) and (b), respectively, where $\sigma$ is the leakage factor, and $\sigma=1-L_M^2/L_s/L_r$.

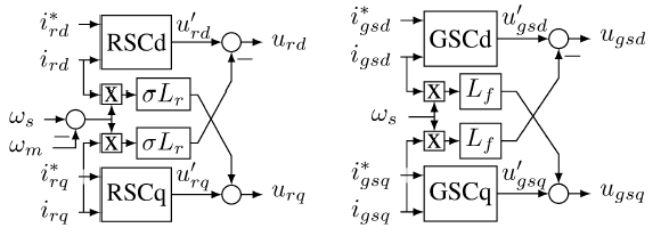


Fig. 4. Control structures of RSC*dq* and GSC*dq* for DFIG. (a) RSC*dq*. (b) GSC*dq*.

The specific implementation of the controllers is detailed as follows.

1) Two-degree-of-freedom (2-DOF) PI regulator: the inner-loop controllers including RSC*dq*, GSC*dq*, and VDC take the form of (13)

$$C_{\mathrm{PI}}(s)=K_p(br-y)+\frac{K_i}{s}(r-y) \tag{13}$$

where $r$ is the setpoint of the controlled variable; $y$ is the measured feedback value of the controlled variable ; $b$ is the setpoint weighting factor; and $K_p$ and $K_i$ are the proportional and integral gains, respectively.

2) VSM implementation: the VSM control logic implemented in this paper follows the "Alternative I" configuration in [6], but with the following two key refinements. ① a full per-unit formulation for all VSM parameters and signals; and ② an additional damping term $D_d$ applied directly to the virtual shaft torque to tackle the electromechanical oscillations [26].

The scaling factor $\omega_b$ (base angular frequency) in certain integrators shown in Fig. 3 is a requisite of the per-unit implementation.

## III. Initial Tuning

### A. Design Assumptions for Initial Tuning

The initial tuning of controllers in DFIG is carried out by treating each controller in isolation and ignoring any controller interaction. This is common in industry [1], [6], [26], and some design assumptions are given as follows.

1) No loop interaction: the inner control loops (e.g., current controllers) are presumed to be significantly faster than outer control loops (e.g., power or voltage controllers). Consequently, the inner control loops are considered to have an infinitely fast response during the tuning of the outer control loops. Conversely, the outer control loops are considered to provide constant setpoints during the tuning of inner control loops. Furthermore, each of the four DFIGs is tuned independently, without considering the inter-machine controller interaction.

2) Designated operating point: the controllers are tuned at the designated operating point, where the grid absorbs 0.7 p.u. of the rated active power for wind farm (i.e., $P_{\mathrm{grid}}=0.7$ p.u.), $SCR=1$, $|v_g|=1$ p.u., and $f=1$ p.u. Besides, all DFIGs are equally loaded.

3) Reference design rules for different controllers: ① the virtual-shaft controller of VSM for active power and virtual-flux controller of VSM for reactive power, which are shorted as VSMP and VSMQ for simplicity, follow the design in [6] and [26]; ② the virtual impedance, part of the VSM strategy, is selected according to [6]; ③ each 2-DOF PI regulator in RSC$dq$, GSC$dq$, and VDC are tuned using the pole placement technique, and $b=1$ is used for (13).

Neglecting the controller interaction, the initial tuning aims to achieve a standard second-order closed-loop transfer function for each PI-controlled subsystem, as discussed in [1].

### B. Initial Specifications and Ideal Design Targets

Table I includes the initial controller specifications and ideal design targets for each controller, as defined during the ideal tuning, where $t_s^{\%}$ is the settling time within a specified percentage tolerance band; $\zeta$ is the desired damping ratio; $\omega_n$ is the equivalent closed-loop natural frequency; and $\varphi_m$ and $\omega_o$ are the open-loop phase margin and gain-crossover frequency, respectively.

TABLE I
Initial Specifications and Ideal Design Target for Each Controller

| Controller | Initial specification | | Ideal design target | | |
|---|---|---|---|---|---|
| | $t_s^{\%}$ (s) | $\zeta$ | $\omega_n$ (rad/s) | $\varphi_m$ (°) | $\omega_o$ (rad/s) |
| VSMP | 1 | 0.707 | 5.65 | 67.2 | 8.07 |
| VSMQ | 2 | | | 90.0 | 2.00 |
| RSC$dq$ | 0.004 | 0.707 | 1414 | 65.7 | 2184.00 |
| VDC | 0.080 | 0.707 | 70.4 | 65.5 | 109.90 |
| GSC$dq$ | 0.004 | 0.707 | 1414 | 65.7 | 2184.00 |

## IV. Intra-machine Controller Interactions

To test the validity of the design assumptions in Section III, a frequency-domain framework is designed to: ① isolate each individual controller within the complete and coupled multi-machine system; ② derive its true local open-loop transfer function, accounting for all interactions; and ③ quantify the strength of the dynamic intra-machine controller interactions.

### A. General Multi-loop Control Formulation

Figure 5 illustrates a general control architecture for interaction analysis, with notation and framework used in well-established multi-loop control system design literature [23].

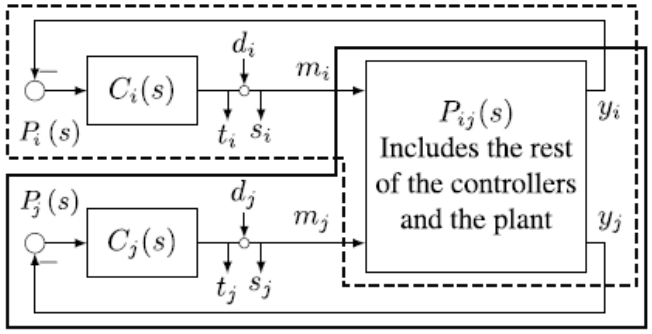


Fig. 5. General multi-loop control architecture for interaction analysis.

Controllers $C_i$ and $C_j$ generate manipulated variables $m_i$ and $m_j$, respectively, which are inputs to plant block $P_{ij}$. $P_{ij}$ encapsulates the physical subsystem and all other active controllers, thus embedding the dynamic intra-machine controller interactions. The auxiliary perturbation signals $d_i$ and $d_j$ are introduced at the controller output terminal, and their corresponding effects are measured by the sensor output pairs $(s_i, t_i)$ and $(s_j, t_j)$. This setup allows for the computation of standard sensitivity $S_i(s)=s_i(s)/d_i(s)$ and complementary sensitivity $T_i(s)=-t_i(s)/d_i(s)$ functions for each control loop $i$, while the other control loops remain closed, without altering the original closed-loop control structure:

$$\begin{cases} S_i(s)=\dfrac{1}{1+C_i(s)P_i(s)} \\ T_i(s)=\dfrac{C_i(s)P_i(s)}{1+C_i(s)P_i(s)} \end{cases} \tag{14}$$

where $P_i(s)$ is the transfer function of plant perceived by controller $C_i$, with $m_i$ as its input and $y_i$ as its output.

The local open-loop transfer function for control loop $i$ is $G_i(s)=C_i(s)P_i(s)$, which equals $T_i(s)/S_i(s)$. The control loop $i$ is considered robustly decoupled if $G_i(s)$ satisfies the phase margin requirements, even while all other controllers remain active and dynamically interacting.

### *B. One-degree-of-freedom (1-DOF) Controllers for Loop Shaping*

The classical frequency-domain loop-shaping techniques are most directly applied to 1-DOF controllers. Therefore, the 2-DOF PI regulator used in the hierarchical control structure of DFIG must be reconfigured.

1) RSC*dq*, GSC*dq*, and VDC: for the 2-DOF PI regulators used in controllers including RSC*dq*, GSC*dq*, and VDC, $b$ in (13) is fixed at 1.

2) VSMP: the VSMP incorporates a steady-state droop characteristic, which is typically mandated by grid codes and thus is considered a fixed parameter. To facilitate the loop shaping, the droop gain $D_p$ is factored out of the main control loop, as illustrated in Fig. 6, and the term $D_d/(2H)$ is linked to the error between $P^*/\omega_s^0$ and $P/\omega_s^0$ and can be changed to only link $-P/\omega_s^0$ via a switch. VSMP within the dashed box is a 1-DOF controller $C_{\text{VSMP}}(s)$ with steady-state gain of 1 (independent of Dp), while the overall steady-state gain, before the angle of the stator voltage ($\delta_s$) is calculated, remains $1/D_p$.

$$C_{\text{VSMP}}(s)=\frac{1+sD_d}{1+s\left(2H/D_p\right)} \tag{15}$$

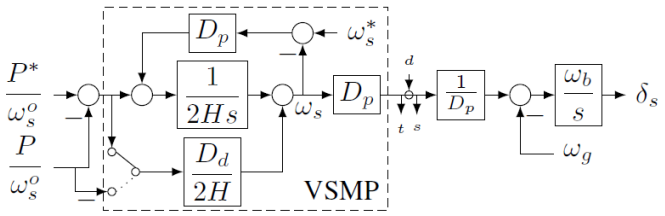


Fig. 6. Structure of VSMP with 1-DOF controller.

3) VSMQ: similar to the $D_p$ in VSMP, the droop gain $D_q$ in VSMQ is a fixed parameter. Consequently, only the proportional gain $K_q$ is a design variable for loop shaping. The output of the integrator, $(1/\omega_b)(d\psi_{vd}/dt)$, is taken as the manipulated variable $m$ and the integrator block $\omega_b/s$ is considered part of the plant. This configuration yields an explicit 1-DOF proportional controller $K_q$.

### *C. Determination of Plant and Stability Margins*

For each controller in the DFIG, we determine: ① $P_i(s)$, and ② the stability margins, i.e., $\varphi_m$ and $\omega_o$, of each open loop. This computation is carried out using MATLAB/Simulink in four steps (Version R2024a or later is recommended for compatibility with the described linearisation tools).

1) Designated operating point: the *findop* command in Simulink is used to set the non-linear model of wind farm to the designated operating point defined in Section III, i.e., $P_{\text{grid}}=0.7$ p.u., $|v_g|=1$ p.u., and $SCR=1$. Accurate steady-state conditions $[x^\star, u^\star]$ can be found if a strict tolerance is used (e.g., $\|\dot{x}^\star\|_2<10^{-8}$), where $x^\star$ is the state vector at the designated operating point; and $u^\star$ is the input vector computed by *findop* to drive the non-linear model of wind farm to the designated operating point.

2) Full small-signal linearisation and input/output (I/O) extraction: all the designed perturbations $d_i$ and their associated sensor output pairs $(s_i, t_i)$ are set as the linear analysis points in the Simulink model. A single execution of the *linearize* command in Simulink produces the state-space realisation of the entire closed-loop multi-machine system, which constitutes the full linearised model, by using the defined I/Os and the obtained operating point. Subsequently,

① The sensitivity path from $d_i$ to $s_i$ is extracted from the full linearised model to obtain $S_i(s)$.

② Similarly, the complementary-sensitivity path from $d_i$ to $t_i$ is extracted from the full linearised model to obtain $T_i(s)$.

③ $G_i(s)$ is computed using (14).

④ Since $C_i(s)$ is known analytically, $P_i(s)$ is calculated as $P_i(s)=G_i(s)/C_i(s)$.

3) Stability margin calculation: the standard *margin* command in Simulink is applied to $G_i(s)$ to yield the actual values $\varphi_m$ and $\omega_o$.

The values of $\varphi_m$ and $\omega_o$ at different stages are presented in Table II, where Stage A represents the ideal design targets derived from Table I, Stage B shows the actual results of initial tuning based on the full linearised model, and Stages $\Gamma_1$-$\Gamma_3$ represent the results with the redesign procedure with 1-3 iterations, respectively, which will be detailed in Section V. For the time being, Stage B clearly reveals the inadequacy of the initial tuning. Most notably, the phase margins of RSC*dq* collapse.

### *D. Interaction Indices and Derivation of Redesign Sequence*

A quantitative metric is needed to capture how strongly each control loop influences others and, conversely, how sensitive it is to disturbances propagating from other control loops. The following procedure is proposed for the calculation of these interaction indices:

1) A unit impulse perturbation signal $d_i$ is injected at the design input of control loop $i$, while all other perturbation signals $d_j$ $(j\neq i)$ are maintained at zero.

2) The time-domain perturbation-rejection signals are recorded over a defined interval (0-$t_f$), where $t_f=1$ s: $\sigma_i^{(i)}(t)\triangleq s_i(t)$, which represents the response of control loop $i$ to its own perturbation, and $\sigma_j^{(i)}(t)\triangleq s_j(t)$ $(j\neq i)$, which represents the response of control loop $j$ for the perturbation in control loop $i$.

The directional correlation coefficient $\rho_{ij}$ from the perturbed control loop $i$ to an observed control loop $j$ can be de-

TABLE II
VALUES OF $\varphi_m$ AND $\omega_o$ AT DIFFERENT STAGES

| controller | Stage A | | Stage B | | Stage $\Gamma_1$ | | Stage $\Gamma_2$ | | Stage $\Gamma_3$ | |
|---|---|---|---|---|---|---|---|---|---|---|
| | $\varphi_m$ (°) | $\omega_o$ (rad/s) | $\varphi_m$ (°) | $\omega_o$ (rad/s) | $\varphi_m$ (°) | $\omega_o$ (rad/s) | $\varphi_m$ (°) | $\omega_o$ (rad/s) | $\varphi_m$ (°) | $\omega_o$ (rad/s) |
| VSMP | 67.2 | 8.07 | 86.6 | 12.4 | 61.3 | 8.8 | 65.2 | 7.9 | 67.6 | 8.0 |
| VSMQ | | 2.00 | 105.0 | 2.7 | 104.3 | 2.1 | 104.3 | 2.0 | 104.3 | 2.0 |
| RSC*d* | 65.7 | 2184.00 | 15.7 | 332.0 | 65.4 | 2318.0 | 66.1 | 2202.0 | 65.8 | 2184.0 |
| RSC*q* | 65.7 | 2184.00 | 14.7 | 339.0 | 64.4 | 2098.0 | 65.5 | 2175.0 | 65.7 | 2184.0 |
| VDC | 65.5 | 109.90 | 64.5 | 122.7 | 65.5 | 109.9 | 65.5 | 109.9 | 65.5 | 109.9 |
| GSC*d* | 65.7 | 2184.00 | 47.0 | 1050.0 | 64.8 | 2170.0 | 65.7 | 2184.0 | 65.7 | 2184.0 |
| GSC*q* | 65.7 | 2184.00 | 42.3 | 1045.0 | 54.5 | 2372.0 | 65.0 | 2221.0 | 65.7 | 2187.0 |

fined as:

$$\rho_{ij} = \frac{\left| \int_0^{t_f} \sigma_j^{(i)}(t)\sigma_i^{(i)}(t)\,\mathrm{d}t \right|}{\sqrt{\int_0^{t_f} [\sigma_j^{(i)}(t)]^2\,\mathrm{d}t}\ \sqrt{\int_0^{t_f} [\sigma_i^{(i)}(t)]^2\,\mathrm{d}t}} \tag{16}$$

where $0 \le \rho_{ij} \le 1$. A large value of $\rho_{ij}$ indicates that a disturbance primarily handled by control loop $i$ induces a significant time response in control loop $j$, and this response is strongly correlated with the self-response of control loop $i$.

By repeating this impulse-response experiment for each control loop $i$, we can construct the absolute correlation matrix $\boldsymbol{\rho} = [\rho_{ij}]$, which is a square interaction matrix that quantifies the coupling strength between control loops. Figure 7 shows the grey-scale heat maps of absolute correlation matrix $\boldsymbol{\rho}$ when the control loop of each controller in DFIG1 and DFIG3 is perturbed, where darker cells are associated with stronger coupling. Each row in Fig. 7 illustrates the intra-machine controller interactions (i.e., how each controller in DFIG1 or DFIG3 interacts with other controllers inside the same DFIG) based on the absolute correlation matrix. Here, each DFIG has $n$=7 primary controllers, i.e., VSMP, VSMQ, RSC*d*, RSC*q*, VDC, GSC*d*, and GSC*q*.

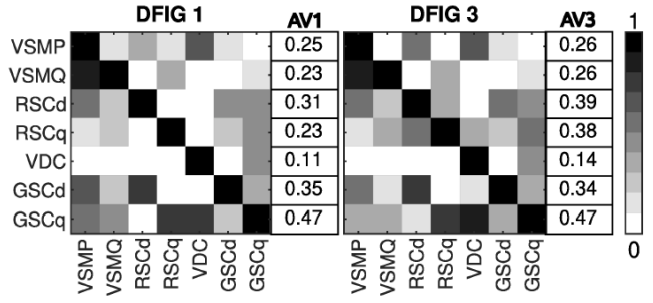


Fig. 7. Grey-scale heat maps of absolute correlation matrix **ρ** when each controller in DFIG1 and DFIG3 is perturbed. (a) DFIG1. (b) DFIG3.

Two quantitative indices can be derived from $\boldsymbol{\rho} = [\rho_{ij}]$: ① influence index (IIdx), defined as the average of off-diagonal elements in row $i$ of $\boldsymbol{\rho}$, which quantifies the effect of perturbed control loop $i$ on other control loops $j \neq i$; and ② sensitivity index (SIdx), defined as the average of off-diagonal elements in column $i$ of $\boldsymbol{\rho}$, which quantifies how strongly control loop $i$ is affected by disturbances originated from other control loops $j \neq i$.

The formulations of IIdx and SIdx are given as (17), where the diagonal elements $\rho_{ii}$ are excluded from both summations to eliminate the self-perturbation response of each controller, ensuring that only the mutual interactions between different control loops are reflected.

$$\begin{cases} IIdx_i = \dfrac{1}{n-1} \displaystyle\sum_{j=1, j\neq i}^{n} \rho_{ij} \\ SIdx_i = \dfrac{1}{n-1} \displaystyle\sum_{j=1, j\neq i}^{n} \rho_{ji} \end{cases} \tag{17}$$

The IIdx values for each controller in DFIG1 and DFIG3 have been included in Fig. 7. This enables the observation of diverse intra-machine controller interaction patterns.

A similar study is carried out to investigate the inter-machine controller interactions, i.e., the effect of a controller in one machine on another controller in a different machine, although an in-depth analysis of this point is beyond the scope of this paper. A grey-scale heat map characterising the inter-machine controller interactions between DFIG1 and DFIG3 is shown in Supplementary Material A.

### *E. Prioritised Redesign Sequence*

The redesign of controllers should prioritise those control loops that exert the strongest overall influence on the remaining control loops, as mitigating their disruptive impact first can simplify the subsequent tuning of other, less influential, or more sensitive ones. By sorting the IIdx values for controllers in DFIG1 and DFIG3 in descending order, the following optimal redesign sequence is proposed:

$$\mathrm{GSC}q \rightarrow \mathrm{GSC}d \rightarrow \mathrm{RSC}d \rightarrow \mathrm{RSC}q \rightarrow \mathrm{VSMP} \rightarrow$$
$$\rightarrow \mathrm{VSMQ} \rightarrow \mathrm{VDC}$$

Note that the *d*- and *q*-axis variables of the same controller are grouped in the sequence.

### *F. Time-domain Confirmation*

To corroborate the frequency-domain findings regarding intra-machine controllers and stability margin degradation, the step response tests are conducted on setpoint input using the full linearised model. Figure 8 compares the ideal step response at Stage A and actual step responses at Stage B.

The comparison in Table II and Fig. 8 has the following findings.

1) Conservative VSMP design: considering the full coupling, i.e., at Stage B, the VSMP actually shows a lower

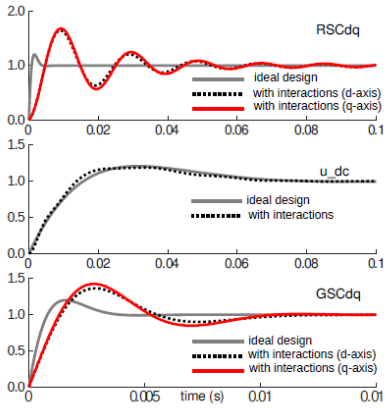


Fig. 8. Comparison of ideal step response at Stage A and actual step responses at Stage B. (a) RSC*dq*. (b) VDC. (c) GSC*dq*.

overshoot and a faster settling time than originally specified. The phase margin increases from 67.2° to 86.6°, and the gain-crossover frequency grows from 8.07 to 12.4 rad/s, indicating that the initial tuning is conservative and the VSMP is more robust than required.

2) Directional coupling from GSC*dq* to RSC*dq*: as shown in Fig. 7, the paths GSC*dq*→RSC*dq* are markedly darker than the reverse direction, indicating that GSC*dq* strongly affects RSC*dq*. At Stage B, as shown in Fig. 8, a pronounced 50 Hz oscillation is produced in the step response of RSC*dq*, and it quantitatively corresponds to the collapse of phase margin of RSC*dq*.

3) Moderate damping loss in GSC*dq*: as shown in Table II, compared with Stage A, GSC*dq* at Stage B exhibit a phase margin reduction, which is consistent with the weaker coupling in the direction of RSC*dq*→GSC*dq* shown in Fig. 7. It confirms the asymmetric interaction between rotor- and grid-side current control.

4) Robustness of VSMQ and VDC: compared with Stage A, VSMQ exhibits an increase in phase margin at Stage B, rising from 90° to 105°. The VDC similarly retains a high phase margin, with only a marginal decrease from 65.5° to 64.5°. As shown in Fig. 8, the actual step response of VDC at Stage B remains well within the ideal one at Stage A. Both VSMQ and VDC are inherently robust and largely decoupled from the more critical interactions affecting RSC*dq* and GSC*dq*.

5) Methodology validation: the strong alignment of ① the analytical stability margin reduction (see Stage B at Table II), ② the quantified coupling strengths from the absolute correlation matrix $\boldsymbol{\rho}$ (see Fig. 7), and ③ the observed oscillations and deviations (see Fig. 8) demonstrates the consistency and predictive power of the multi-loop control architecture for interaction analysis.

6) Need for coordinated redesign: the redesign sequence in Section IV-E provides a clear path towards performance recovery. Unlike a formal $\mu$-analysis, the dominant interaction pathways at the designated operating point are identified and quantified.

## V. Coordinated Multi-loop Control Design

### Methodology

This section illustrates the coordinated multi-loop control design methodology based on classical frequency-domain loop-shaping techniques, starting from a controller design that ignores possible controller interactions. The redesign procedure relies on the interaction analysis and the prioritised redesign sequence in Section IV, and is applied iteratively to each controller to ensure that the design outcomes closely match the ideal design targets.

Here, only the redesign of one critical controller for DFIG1, i.e., RSC*q*, is detailed as an example. The same systematic steps are applied to all other controllers according to the derived priority order. The redesign for RSC*q* of DFIG1 comprises the following steps.

1) Controller selection and I/O tagging for analysis: to analyse the RSC*q* of DFIG1, a linear analysis point is inserted at the terminal of its manipulated variable output ($u'_{rq}$ in Fig. 4(a)), which serves as the perturbation injection point *d*. The signals immediately before (controller output) and after (plant input considering the summation node) this injection point are tagged as *s* and *t*, respectively, for sensitivity function extraction. By letting $b=1$, the nominal PI law for this 1-DOF controller is given by:

$$C_{\mathrm{RSC}q}(s)=K_{p,\mathrm{RSC}q}+\frac{K_{i,\mathrm{RSC}q}}{s} \tag{12}$$

where $K_{p,\mathrm{RSC}q}$ and $K_{i,\mathrm{RSC}q}$ are the proportional and integral gains of RSC*q*, respectively.

2) Extraction of the actual plant and current open-loop response: using the full linearised model, the sensitivity functions $S(s)$ and $T(s)$ for RSC*q* are computed, and the current open-loop transfer function $G(s)$ and the actual plant $P(s)$ seen by $C_{\mathrm{RSC}q}(s)$ can be determined:

$$\begin{cases} G(s)=\dfrac{T(s)}{S(s)} \\ P(s)=\dfrac{G(s)}{C_{\mathrm{RSC}q}(s)} \end{cases} \tag{13}$$

3) Redesign targets: the objective is to reshape $G(s)$ to achieve the ideal design targets at Stage A for RSC*q*, i.e., a crossover frequency of $\omega_o=2184$ rad/s and a phase margin of $\varphi_m=65.7°$. To design the new PI controller, we first obtain the frequency response of the identified plant $P(\mathrm{j}\omega_o)$ ($s=\mathrm{j}\omega_o$) at the target crossover frequency $\omega_o$, yielding the magnitude and phase of $A_p=-10$ dB and $\phi_p=-93.8°$, respectively.

4) Computation of new PI controller parameters: the new PI controller $C_{\mathrm{RSC}q,\mathrm{new}}(s)$ must provide a gain contribution of $\Delta A=-A_p=+10$ dB and a phase shift of $\Delta\phi=\varphi_m-(180°+\phi_p)=65.7°-(180°-93.8°)=-20.5°$ at $s=\mathrm{j}\omega_o$. two equations for $\Delta A$ and $\Delta\phi$ are given with two unknown variables $K_{p,\mathrm{RSC}q}$ and $K_{i,\mathrm{RSC}q}$. Once the new PI controller parameters $K_{p,\mathrm{RSC}q,\mathrm{new}}$, $K_{i,\mathrm{RSC}q,\mathrm{new}}$ are calculated, they are implemented in all machines.

5) Verification of redesigned controller: with $K_{p,\mathrm{RSC}q,\mathrm{new}}$ and $K_{i,\mathrm{RSC}q,\mathrm{new}}$ in all machines, the reshaped open-loop transfer function $G_{\mathrm{rd}}(j\omega)=C_{\mathrm{RSC}q,\mathrm{new}}(\mathrm{j}\omega)P(\mathrm{j}\omega)$ should have a phase margin and a crossover frequency close to the ideal design targets.

The same steps are systematically applied to all seven controllers of each DFIG in the wind farm, following the prioritised sequence. At Stage $\Gamma_1$, the results with only one iteration are obtained, as shown in Table II, with stability margins close to the ideal design targets.

This iterative process may continue until all controllers achieve their ideal design targets. To illustrate the convergence, the proposed methodology is carried out with three iterations at the designated operating point. After each iteration, the phase margin and gain-crossover frequency are re-evaluated, the results of which with 1-3 iterations, i. e., at Stages $\Gamma_1$-$\Gamma_3$, are shown in Table II.

Define the maximum relative errors for both $\varphi_m$ and $\omega_o$ across all controllers at iteration $k$ as and $e_{\omega_o,k}$, respectively:

$$e_{\varphi_m,k} = \max_i \left| \frac{\varphi_{m,i}^{(k)} - \varphi_{m,i}^{\text{target}}}{\varphi_{m,i}^{\text{target}}} \right| \times 100\% \tag{14}$$

$$e_{\omega_o,k} = \max_i \left| \frac{\omega_{o,i}^{(k)} - \omega_{o,i}^{\text{target}}}{\omega_{o,i}^{\text{target}}} \right| \times 100\% \tag{15}$$

where the superscript target represents the ideal design target

Note that the VSMQ is excluded from $e_{\varphi_m,k}$ calculation, as it has no $\varphi_m$ target.

The rates of convergence obtained in Table III show a rapid reduction in $e_{\varphi_m,k}$ from 17.2% to 0.6% and $e_{\omega_o,k}$ from 9.0% to 1.2% for crossover frequencies. Notably, GSC$q$ exhibits the largest initial errors in both metrics, validating its identification as the most influential controller in the prioritised redesign sequence. VSMP shows a steady decrease in errors across subsequent iterations, further confirming that the proposed methodology effectively improves the dynamic performance of all targeted controllers.

TABLE III
RATES OF CONVERGENCE

| Controller | Iteration | $e_{\varphi_m,k}$ (%) | $e_{\omega_o,k}$ (%) |
|---|---|---|---|
| GSC$q$ | 1 | 17.2 | 9.0 |
| VSMP | 2 | 3.0 | 2.5 |
| | 3 | 0.6 | 1.2 |

The flowcharts summarising the redesign for all controllers can be found in Supplementary Material A.

## VI. RESULTS AND VALIDATION

### A. Frequency-domain Performance

The effectiveness of the proposed methodology is confirmed by comparing $\varphi_m$ and $\omega_o$ at Stage $\Gamma_1$ with those at Stage A and Stage B. Further redesign iterations could progressively drive $(\varphi_m, \omega_o)$ pairs even closer to the setpoints specified in Stage A.

While this study focuses on achieving nominal performance targets, a formal robust stability analysis (e. g., using $\mu$-analysis or Monte Carlo simulations with parameter uncertainties) would be a valuable extension for industrial applications and is considered for future work.

### B. Simulation of Small- and Large-disturbance Response

Figure 9 compares the ideal unit-step responses at Stage A and actual unit-step responses after the redesign procedure with one iteration at Stage $\Gamma_1$ for RSC$dq$ and GSC$d$.

The redesigned controllers demonstrate excellent setpoint tracking performance, closely aligned with the ideal unit-step response. This is in sharp contrast to the results in Fig. 8, where the interactions are ignored at the design stage. Small deviations will be further attenuated and typically vanish after a second redesign cycle.

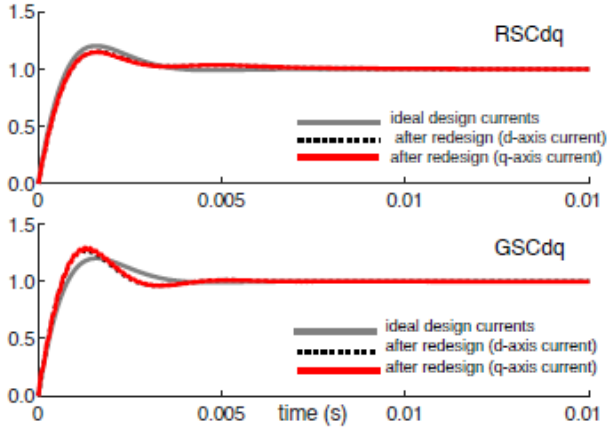


Fig. 9. Comparison of ideal unit-step response at Stage A and actual unit-step response after redesign with one iteration at Stage $\Gamma_1$ for RSC$dq$ and GSC$dq$.

The unit-step responses for controllers at different operating points are simulated. The different operating points considered are chosen at the boundary of the expected working region of DFIG. Details of the operating points are shown in Table IV.

TABLE IV
DETAILS OF OPERATING POINTS

| Operating point | $V_{pcc}$ (p.u.) | $P$ (p.u.) | $SCR$ |
|---|---|---|---|
| 1 | 0.95 | 0.50 | 1.0 |
| 2 | 0.95 | 0.50 | 3.0 |
| 3 | 0.95 | 0.75 | 1.0 |
| 4 | 0.95 | 0.75 | 3.0 |
| 5 | 1.05 | 0.50 | 1.0 |
| 6 | 1.05 | 0.50 | 3.0 |
| 7 | 1.05 | 0.75 | 1.0 |
| 8 | 1.05 | 0.75 | 3.0 |

As shown in Fig. 10, the unit-step responses of RSC$dq$ and GSC$dq$ at operating points 1-8 do not change much compared with those at the designated operating point shown in Fig. 9. However, more differences appear in the unit-step responses of active and reactive power delivered from DFIG1 at operating points 1-8, as shown in Fig. 11. Note that, for a grid with $SCR = 1$, the maximum value of active power $P$ delivered to the grid is 0.75 p.u.. This is because larger values will lead to positive real eigenvalues of the linear system,

thereby resulting in system instability, which is closely associated with the instability of PCC voltage $V_{pcc}$.

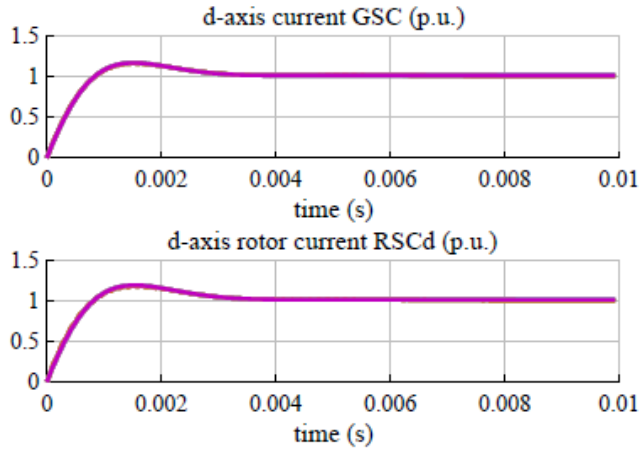


Fig. 10. Unit-step response of RSC*dq* and GSC*dq* at operating points 1-8.

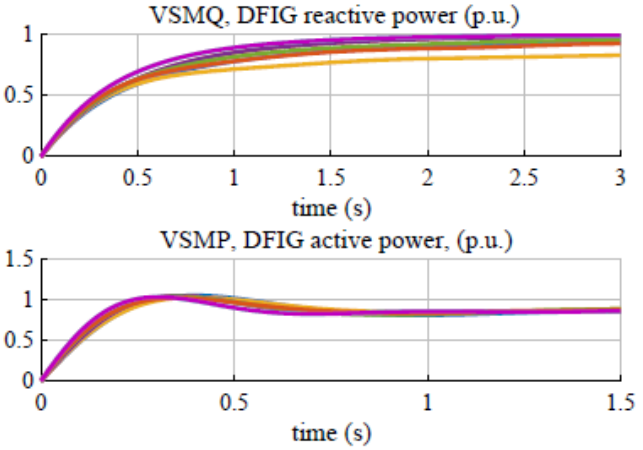


Fig. 11. Unit-step response of active and reactive power delivered by DFIG1 at operating points 1-8.

Time-domain simulations, with large-signal disturbances, are performed on the non-linear Simulink model of wind farm. For the remainder of this paper, frequency-response design (FRD) refers to the controllers obtained through the proposed methodology, while the time-response design (TRD) refers to the controllers based on the initial tuning. Each simulation scenario begins at the designated operating point.

*1) Active Power Setpoint Step*

Figure 12 illustrates the rotor-turbine speed deviation ($\Delta\omega=\omega_r-\omega_t$) with active power setpoint step of 0.2 p.u. in DFIG1 at $t=1$ s. This deviation would produce a drivetrain torsional deformation. FRD reduces the initial overshoot and the final settling time. This should translate in reduced mechanical stress on the turbine drivetrain.

*2) Voltage dip*

Figure 13 plots the DC-link voltage of DFIG1 and the *q*-axis GSC current during a voltage dip of 0.2 p.u. at the grid bus at $t=1$ s for 0.5 s. FRD also reduces the DC-link and *dq*-axis oscillations. This should lead to a faster post-fault recovery.

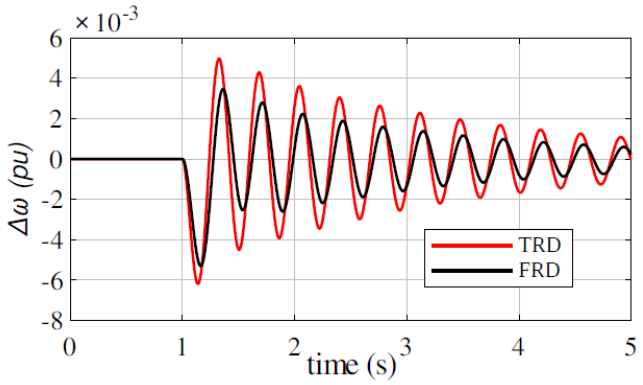


Fig. 12. Rotor-turbine speed deviation with active power setpoint step of 0.2 p.u. in DFIG1 at $t=1$ s.

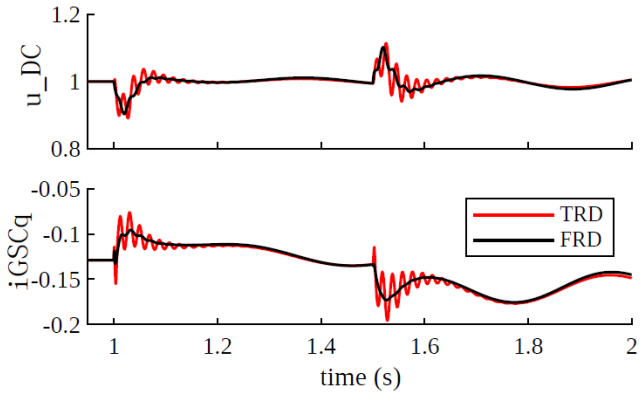


Fig. 13. DC-link voltage and *q*-axis GSC current for DFIG1 during a voltage dip of 0.2 p.u. at the grid bus at $t=1$ s for 0.5 s.

## VII. Quantifying Performance Improvements

A number of performance metrics related to the controller performance are evaluated in DFIG1 at the designated operating point, and the results are recorded in Table V, where all metrics are referred to the close-loop response of different controllers.

1) The maximum sensitivity $\|S\|_\infty$: robustness to output disturbances. Lower values indicate better performance, and the target is $\|S\|_\infty<6$ dB.

2) The maximum complementary sensitivity $\|T\|_\infty$: robustness to noise. Lower values indicate better performance, and the target is $\|T\|_\infty<2$ dB.

3) Overshoot: the maximum overshoot percentage in the step response. Lower values are preferable.

3) Peak time: time to reach the maximum overshoot. Related to speed of response.

## VIII Conclusion

Based on classical frequency-domain loop-shaping techniques, this paper presents a coordinated multi-loop control design methodology for VSM-controlled DFIGs in a wind farm. By explicitly accounting for intra-machine controller interactions, the proposed methodology achieves the design

TABLE V
COMPARISON OF PERFORMANCE METRICS RELATED TO CONTROLLER PERFORMANCE

| Controller | $\|S\|_\infty$ (dB) | | | $\|T\|_\infty$ (dB) | | | Overshoot (%) | | Peak time (s) | |
|---|---|---|---|---|---|---|---|---|---|---|
| | TRD | FRD | Difference | TRD | FRD | Difference | TRD | FRD | TRD | FRD |
| VSMP | 0.79 | 0.21 | 0.58 | 0.11 | 0.96 | -0.85 | 8.51 | 18.03 | 0.2950 | 0.3745 |
| VSMQ | 0.21 | 0.01 | 0.19 | 0.00 | -0.00 | 0.00 | 0.00 | 0.00 | | |
| RSC$d$ | 14.90 | 3.17 | 11.73 | 14.65 | 1.55 | 13.10 | 64.85 | 18.10 | 0.0091 | 0.0015 |
| RSC$q$ | 14.90 | 2.41 | 12.49 | 14.65 | 1.54 | 13.10 | 64.85 | 18.09 | 0.0091 | 0.0016 |
| VDC | 1.28 | 0.72 | 0.56 | 1.99 | 1.94 | 0.05 | 18.94 | 19.40 | 0.0334 | 0.0319 |
| GSC$d$ | 5.43 | 1.59 | 3.84 | 7.83 | 1.34 | 6.49 | 36.45 | 16.38 | 0.0029 | 0.0015 |
| GSC$q$ | 5.43 | 3.60 | 1.83 | 7.83 | 1.43 | 6.40 | 36.45 | 18.56 | 0.0029 | 0.0016 |

Note: the difference means the value of TRD minus that of FRD.

targets and high-performance operation under both small-signal and large-signal disturbances, even in weak grids (e.g., $SCR = 1$).

The systematic application of the perturbation-rejection signals identifies and quantifies the interactions among controllers in a DFIG-based wind farm and reveals severe phase margin reduction in critical controllers such as RSC$q$ when using initial tuning. However, a single iteration of the redesign procedure restores all stability margins to nearly their ideal design targets. The step responses derived from the full linearised model of the wind farm closely matches the ideal design targets. Finally, the non-linear time-domain simulations with the full linearised model further confirms the improved performance of the controllers tuned via the proposed methodology compared with that ignoring the intra-machine controller interactions.

A key advantage of the proposed methodology is its reliance on well-established frequency-domain metrics and standard linear analysis tools readily available in commercial simulation-and-design packages (e.g., MATLAB/Simulink).

From a theoretical perspective, further work is needed on several points.

1) The design procedure taking into account a rich set of possible operating points and grid parameters (e.g., different $Z_{grid}$ values) need to be generalised, and an optimisation problem should be formulated to systematically select phase margins and gain-crossover frequencies.

2) The analysis and design procedures need to be extended to minimise the effects of the inter-machine controller interactions of the wind farm, as the same controller design is currently implemented in all machines.

3) The analysis and design procedures to minimise the effects of the interactions between controllers in the wind farm and external devices (e.g., STATIC compensators or synchronous generators).

The case study used in this paper has been coded in MATLAB using a vectorised description in which all elements of the same type can be put together in the same subroutine, even if they have different parameters. This approach is very similar to the one in [26], where the use of large system models has been successfully explored, although model reduction techniques will be investigated in the future. From an application perspective, testing the redesigned controllers in an experimental set-up will be pursued to assess the impact of real-world factors.

## REFERENCES


[1] G. Abad, J. López, M. Rodríguez *et al.*, *Doubly Fed Induction Machine: Modeling and Control for Wind Energy Generation*. Chichester: John Wiley & Sons, 2011.

[2] P. Jacob and R. Teodorescu, "Inertia emulation capability of DFIG wind turbines," *Electric Power Systems Research*, vol. 123, pp. 229-236, Jun. 2015.

[3] B. Wen, D. Boroyevich, and R. Burgos, "Small-signal stability of ac systems with multiple converters," *IEEE Transactions on Power Electronics*, vol. 33, no. 1, pp. 45-60, Jan. 2018.

[4] J. Rocabert, A. Luna, F. Blaabjerg *et al.*, "Control of power converters in ac microgrids," *IEEE Transactions on Power Electronics*, vol. 27, no. 11, pp. 4734-4749, Nov. 2012.

[5] Q. Zhong and G. Weiss, "Synchronverters: inverters that mimic synchronous generators," *IEEE Transactions on Industrial Electronics*, vol. 58, no. 4, pp. 1259-1267, Apr. 2011.

[6] A. González-Cajigas, E. Bueno, J. Roldán-Pérez *et al.*, "Control choices to allow the parallel operation of grid-forming type-III wind turbines," *IEEE Transactions on Power Electronics*, vol. 38, no. 12, pp. 15353-15364, Dec. 2023.

[7] I. Navarro, A. Luna, and F. Dörfler, "Grid-forming control of DFIGs: a small-signal perspective," *IEEE Transactions on Power Systems*, vol. 34, no. 6, pp. 4792-4805, Nov. 2019.

[8] IEEE PES SSO Task Force, "Real-world sub-synchronous oscillations in converter-dominated grids," *IEEE Power & Energy Society Technical Report*, 2023.

[9] J. Sun, "Impedance-based stability criterion for grid-connected inverters," *IEEE Transactions on Power Electronics*, vol. 26, no. 11, pp. 3075-3078, Nov. 2011.

[10] C. Li, F. Dörfler, and M. Krstic, "Frequency and voltage stability of grid-forming vsgs attached to weak grids," *IEEE Journal of Emerging and Selected Topics in Power Electronics*, vol. 10, no. 3, pp. 2662-2671, Jun. 2022.

[11] Y. Yang, T. K. Vrana, and X. Guillaud, "Virtual inductance control for frequency stabilisation of vsgs," *IEEE Transactions on Industrial Electronics*, vol. 70, no. 1, pp. 441-451, Jan. 2023.

[12] D. Culibrk and N. R. Chaudhuri, "Grid-forming converter control under unequal collector impedances," *IET Renewable Power Generation*, vol. 16, no. 5, pp. 1001-1012, Apr. 2022.

[13] *IEEE standard for interconnection and interoperability of inverter-based resources (IBRs) interconnecting with associated transmission electric power systems* IEEE Standard Std 2800-2022, 2022.

[14] ENTSO-E. (2022, Jun.). Stability management in power electronics dominated systems: a prerequisite to the success of the energy transition. [Online]. Available: https://eepublicdownloads. azureedge. net/clean-documents/Publications/Position% 20papers% 20and% 20reports/220616_entso-e_pp_stability_management.pdf

[15] CIGRE WG C4.49. (2024, Mar.). Multi-frequency stability of converter-based modern power systems. [Online]. Available: https://www.e-cigre.org/zpublications/detail/928-multi-frequency-stability-of-converter-based-modern-power-systems

[16] D.-T. Trinh, Y.-K. Wu, and M.-H. Pham, "A novel optimized parameter tuning algorithm for wind turbine grid-forming control to mitigate

power oscillations," *IEEE Transactions on Sustainable Energy*, vol. 16, no. 3, pp. 2150-2165, Jul. 2025.
[17] M. Chen, D. Zhou, and F. Blaabjerg, "Modelling and assessment of virtual synchronous generator in power systems," *Journal of Modern Power Systems and Clean Energy*, vol. 8, no. 3, pp. 399-411, May 2020.
[18] P. Wang, S. S. Refaat, and B. Fahimi, "Sensitivity-function shaping for converter-based resources," *IEEE Transactions on Industrial Electronics*, vol. 63, no. 3, pp. 1732-1742, Mar. 2016.
[19] N. R. Chaudhuri, D. Majumder, and A. Yazdani, "Robust control of inverter-based resources for power system stability," *IEEE Transactions on Power Systems*, vol. 29, no. 3, pp. 1366-1376, May 2014.
[20] T. V. Cutsem and F. Milano, "Voltage stability of power systems with inverter-based resources: a μ-analysis approach," in *Proceedings of the 2015 IEEE PES General Meeting*, Denver, USA, Jul. 2015, pp. 1-5.
[21] Y. Chen and S. Müller, "Automated μ tuning for grid-forming converters in weak grids: recent advances and comparative analysis," *IEEE Transactions on Smart Grid*, vol. 15, no. 2, pp. 1550-1562, Mar. 2024.
[22] A. Al-Majali and P. Rodriguez, "Time-domain robust optimization for coordinated control of grid-forming DFIGs under uncertainty," *Energies*, vol. 17, no. 3, p. 567, Feb. 2024.
[23] S. Skogestad and I. Postlethwaite, "Design tools for multivariable feedback systems," *Annual Reviews in Control*, vol. 29, pp. 51-62, 2005.
[24] K. Johansson, S. Skogestad, and J. Van de Wal, "Multivariable loop-shaping techniques for wind turbine control," *Control Engineering Practice*, vol. 29, pp. 64-78, Aug. 2014.
[25] J. Roldán-Pérez, A. Rodríguez-Cabero, and M. Prodanovic, "Design and analysis of virtual synchronous machines in inductive and resistive weak grids," *IEEE Transactions on Energy Conversion*, vol. 34, no. 4, pp. 1818-1828, Dec. 2019.
[26] A. Tomás-Martín, C. Zuluaga-Ríos, J. Suárez-Porras *et al.*, "A vector-based flexible-complexity tool for simulation and small-signal analysis of hybrid AC/DC power systems," *Sustainable Energy, Grids and Networks*, vol. 43, p. 101817, Jul. 2025.

**Javier García-Aguilar** received the B.Sc. degree in Electromechanical Engineering and the M. Sc. degree in Industrial Engineering from Universidad Pontificia Comillas, Madrid, Spain, in 2016 and 2018, respectively. He was a Research Assistant at the Institute for Research in Technology of the same university from September 2018 to June 2024, working on power-system-related projects and teaching laboratory sessions. He is currently working at Iberdrola Renewables, Madrid, Spain. His research interest includes grid integration of renewable energy.

**Aurelio García-Cerrada** received the M.Sc. degree in Electrical Engineering from Universidad Politécnica de Madrid, Madrid, Spain, in 1986, and the Ph.D. degree in Electronic and Electrical Engineering from the University of Birmingham, Birmingham, U.K., in 1991. He is currently a Professor with the Electronics, Control Engineering and Communications Department and a Member of the Institute for Research in Technology (IIT), Universidad Pontificia Comillas, Madrid, Spain. His research interests include power electronics and its application to electric energy system.

**Juan L. Zamora** received the M.Sc. and Ph.D. degrees from Universidad Pontificia Comillas, Madrid, Spain, in 1991 and 1997, respectively. He was a Postgraduate Student with the Institute for Research in Technology (IIT), Universidad Pontificia Comillas, from 1991 to 1997. Since 1997, he has been a Member of the Research Staff of the IIT, and a Lecturer with the Department of Electronics, Control Engineering and Communications, Universidad Pontificia Comillas. His research interests include control engineering, power electronics, and robotics.

**Emilio J. Bueno** received the Ph.D. degree in electronics engineering from the University of Alcalá, Madrid, Spain, in 2005. Since 2019, he has been a Full Professor with the Department of Electronics at University of Alcalá and a Co-supervisor of the Research Group on electronics engineering applied to renewable energies at the university. His research interests include linear control of grid converter, power quality, distributed generation system, and medium-voltage converter topology.

**Elena Saiz** received the M.Sc. and Ph.D. degrees in electrical power systems from Universidad Pontificia Comillas, Madrid, Spain, in 2010 and 2015, respectively. She is currently with Siemens Gamesa Renewable Energy Innovation & Technology S.L, Madrid, Spain. Her research interests include renewable generation integration and wind turbine.

**Almudena Muñoz-Babiano** is a Project Manager and Energy-storage Specialist with over 20 years of experience in R&D projects across the wind-energy, automotive, and power-systems sectors. She currently works at Siemens Gamesa Renewable Energy Innovation & Technology S. L, Madrid, Spain. Her research interests include development of electrical and technology roadmaps for energy storage system.

**Mohammad E. Zarei** received the B.Sc. and M.Sc. degrees in electrical engineering from the University of Tehran, Tehran, Iran, in 2009 and 2013, respectively, and Ph.D. degree from the Department of Electrical and Electronics Engineering, Universidad Politécnica de Madrid, Madrid, Spain, in 2019. He is now with Siemens Gamesa Renewable Energy Innovation & Technology S.L, Madrid, Spain. His current research interests include electrical machine, application of power electronics to renewable energy conversion, control and operation of wind turbine, stability analysis in microgrid, energy management system, and smart grid.